


Experimental and Theoretical Studies of Tailor-made Schiff Bases as Corrosion Inhibitors for Carbon Steel in HCl

Luana B. Furtado^{a*} , Gabriel B. Leoni^b, R. C. Nascimento^c, Pedro Henrique C. Santos^a,
Fábio J. F. S. Henrique^d, Maria José O. C. Guimarães^a, Simone L. D. C. Brasil^b

^aUniversidade Federal do Rio de Janeiro, Escola de Química, Centro de Tecnologia,
Departamento de Processos Orgânicos, Rio de Janeiro, RJ, Brasil.

^bUniversidade Federal do Rio de Janeiro, Escola de Química, Centro de Tecnologia,
Departamento de Processos Inorgânicos, Rio de Janeiro, RJ, Brasil.

^cUniversidade de Évora, Instituto de Investigação e Formação Avançada, Évora, Portugal.

^dUniversidade Federal do Rio de Janeiro, Instituto de Química, Rio de Janeiro, RJ, Brasil.

Received: September 06, 2022; Revised: January 19, 2023; Accepted: February 01, 2023

Strong acids used in industrial applications as cleaning, descaling, among others, can severely damage metallic structures, requiring corrosion inhibitors to diminish or avoid these issues. Since many conventional compounds used for this purpose may result in environmental and human health issues, eco-friendly compounds such as Schiff bases have been recently investigated. The synthesis of three novel Schiff bases (SBs) was confirmed by infrared spectroscopy (FTIR) and hydrogen nuclear magnetic resonance (¹H-NMR). Weight loss measurements were carried out in 1 M HCl over 303K-333K. Furthermore, the combination of these compounds with a surfactant improved the efficiencies, reaching an efficiency of 93%. Optical and scanning electron microscopies confirmed the reduced roughness and pit depths of carbon steel samples. Density-functional theory calculations for neutral forms of SBs revealed that the geometrical and the energetical parameters are similar for the three studied SBs. The geometrical results exhibited more planar structures of protonated species, improving the chemical and physical interactions between aromatic rings and metallic atoms.

Keywords: *Weight Loss, Acid inhibition, Schiff bases, Surfactants.*

1. Introduction

Carbon steel is the most widely used engineering material due to its good mechanical properties and low cost¹⁻³. Nevertheless, steel corrosion remains a serious problem since it is applied in most industrial sectors, where severe conditions such as high temperatures and acidic pH values can increase directly and indirectly the costs related to corrosion⁴. In that sense, corrosion inhibitors represent a common and efficient method to minimize costs related to material degradation in acid cleaning processes⁵⁻⁷.

Among the organic compounds frequently employed in industrial operations (as acid cleaning and pickling), aromatic heterocyclic chains containing N, S, O and π -electrons present great potential to be considered as adsorption corrosion inhibitors. Thus, commercial organic inhibitors are commonly constituted of amides, imidazolines, quaternary nitrogen, polyoxyalkylated amines, salts of nitrogenous molecules with carboxylic acids, nitrogen heterocyclics, or imides, also known as Schiff bases (SB)^{8,9}. The latter are organic compounds containing $R_2C=NR$, which forms a complex with metal ions through coordination bonds¹⁰. They have proved to be cheap starting precursors with a relatively easy synthetic route, high purity, low toxicity, thermal stability, and

eco-friendliness, which encouraged synthesis, structural and anti-corrosion performance studies of new SB compounds¹¹.

Satpadi et al.¹² investigated Schiff bases composed of cinnamaldehyde and three different amino acids with concentrations varying from 0.05 to 1.0 mM, achieving efficiencies above 96% at 333 K after weight loss measurements. Okey et al.¹³ compared four SBs in 1 M HCl from 0.10 to 1.00 mM, achieving efficiencies from 87.33 to 97.02% in polarisation tests. El Aatiaqui et al.¹⁴ studied new Schiff base from Imidazo(1,2-a)pyridine in 1 M HCl by weight loss measurements at 308 K from 10^{-3} to 10^{-5} M, achieving 97% efficiency.

The present work aims to analyze three novel Schiff bases, synthesized and characterized by FTIR and ¹H-NMR, correlating their inhibition efficiencies, obtained through electrochemical and weight loss measurements, not only with uniform corrosion, as most works do, but also with localized corrosion. The SBs were evaluated at the concentrations of 100 and 600 ppm in 1 M HCl, analyzing temperature effects (303 K, 318 K and 333 K). The combination with two surfactants, an ethoxylated nonyl phenol (A1) and an ethoxylated lauryl alcohol (A2), was also investigated. The purpose of studying the possibility of synergism with surfactants lies in the fact that they may increase the SBs miscibility in the acidic media, allowing better surface coverage, and the

*e-mail: luana_bf18@eq.ufjf.br

synergic interaction with the SB, influencing the inhibition efficiency. Scanning electron microscopy and contact angle measurements were employed to understand the organic film (SB + surfactant) deposition on the metallic surface. Additionally, the potential of the novel SBs as corrosion inhibitors for metallic surfaces was analyzed by theoretical calculations based on density functional theory (DFT).

2. Experimental

The experimental procedure employed to obtain the Schiff bases, as well as the characterization and gravimetric corrosion tests steps are summed up in Figure 1.

2.1. Schiff bases synthesis

The experimental procedure herein applied was adapted from the method reported by Elemike et al.^{11,15}. Equimolar amounts of the precursor amines (aniline, o-toluidine and 4-ethylaniline) and the 4-dimethylaminobenzaldehyde (99%, Sigma-Aldrich) were dissolved in absolute ethanol (99.8%, max. 0.01% H₂O), and then mixed with glacial acetic acid. The mixture was heated and refluxed for 2 hours, so the reactions between each aromatic amine and 4-dimethylaminobenzaldehyde, described in Figure 2, could proceed. Afterward, the resulting mixture was recrystallized 3 times with anhydrous ethanol, and the resulting solid was weighed and dried at 313 K until constant weight.

2.2. Characterization

The Schiff bases crystals were analyzed using a Thermo Scientific Nicolet 5 Fourier-transform infrared spectrometer at 293 K. In total, 20 scans were collected with wavelengths ranging from 4000 to 650 cm⁻¹ and a resolution of 4.00 cm⁻¹.

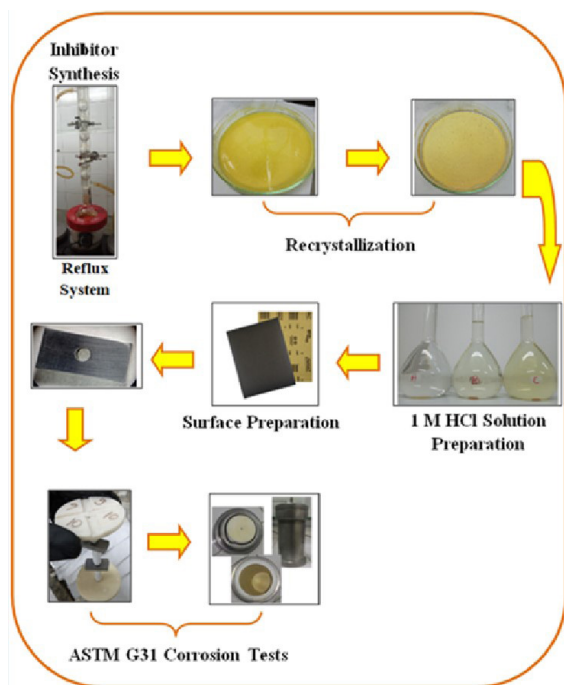


Figure 1. Schiff bases synthesis, characterization, and gravimetric corrosion test steps.

The SBs were also analyzed by Proton Nuclear Magnetic Resonance in a Varian Mercury VX 300 spectrometer at 313 K by dissolving 10-15 mg of the SBs in 0.8 mL of deuterated chloroform (CIL 99.8% d). The observation frequency was 299.99 MHz with 20 scans and an interval between pulses (delay-d1) of 20 s. The obtained data were analyzed with MestreNova 11.04 software version using Fourier Transform.

2.3. Weight loss measurements

Schiff bases inhibition performances were evaluated by weight loss measurements applying replicates, considering the temperature (303 K, 318 K and 333 K) and SBs concentration (100 and 600 ppm) as variables. Also, the synergistic effect between 585 ppm of SB and 15 ppm of surfactants (A1 and A2) was evaluated at 333K. The additive A1, under the commercial name of Renex 65 (HLB (hydrophilic-lipophilic balance) 11.0), is an ethoxylated nonyl phenol (6.5 OE). The hydrophobic part of the molecule comes from a nonylphenol and the hydrophilic part from an ethylene oxide. Additive A2, Unitol L90 (HLB 13.4), is an ethoxylated lauryl alcohol (9 OE), whose hydrophobic part of the molecule is a lauryl alcohol (dodecanol), and the hydrophilic part is an ethylene oxide.

Mild steel (API P110) specimens used in the assays presented the following chemical composition (wt.%): C (0.280), Mn (1.220), Si (0.280), P (0.016), S (0.002), Ni (0.010), Mo (0.110), and Fe (balance). The coupons used for gravimetric tests presented a rectangular shape (8 mm × 20 mm × 5 mm) with a 3 mm diameter central orifice, and were prepared before and after immersion according to ASTM G31 standard practice¹⁶. The gravimetric tests were performed in a 300 mL autoclave for 24 h to calculate the uniform corrosion rate according to ASTM G31, as shown in Equation 1, where K is a constant, Δm is the weight loss of the sample, A is the superficial area, ρ is the density of the sample, and t is the immersion time¹⁶.

$$CR = \frac{K \times \Delta m (g)}{A (cm^2) \times \rho \left(\frac{g}{cm^3} \right) \times t (h)} \quad (1)$$

The inhibiting efficiency (IE_{WL}) was calculated according to Equation 2, where CR_{blank} and CR_{inh} stand for the corrosion rates in the absence and presence of the inhibitor, respectively.

$$IE_{WL} (\%) = \left(\frac{CR_{blank} - CR_{inh}}{CR_{blank}} \right) \times 100 \quad (2)$$

2.4. Electrochemical tests

Carbon steel samples used in electrochemical tests were welded to copper wires and had their lateral and rear surfaces, and electrical connections insulated by epoxy resin. In order to avoid crevice corrosion, prior to immersion, the studied surface was masked with liquid insulating tape, exposing an area of approximately 0.7 cm². Accurate area values were calculated after the essay using the optical microscope Smartzoom 5 (Zeiss).

Electrochemical measurements comprised open-circuit potentials (OCP) monitoring for 120 min, which was experimentally determined in order to reach a steady-state potential condition, followed by electrochemical impedance

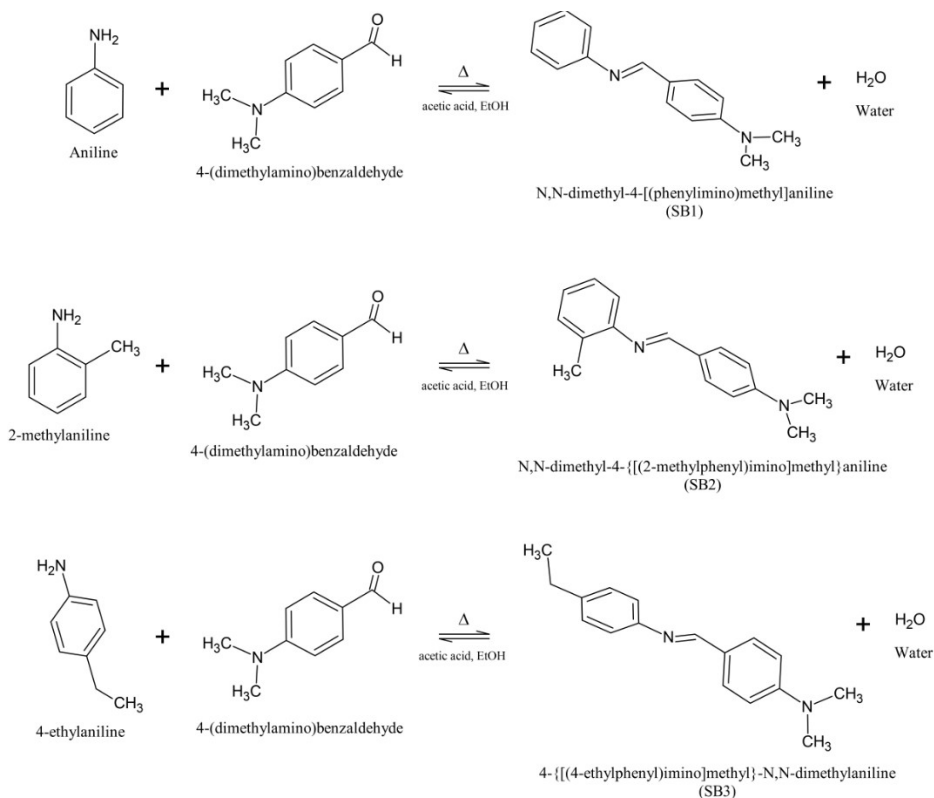


Figure 2. Synthetic route for Schiff bases SB1 (a), SB2 (b) and SB3 (c).

spectroscopy (EIS) and potentiodynamic polarization (PDP). The electrochemical tests were performed at room temperature, by an Autolab Potentiostat/Galvanostat (PGSTAT302N, Metrohm) computer-controlled instrument, with NOVA 2.1 software for electrochemical impedance spectroscopy and potentiodynamic polarization. A three-electrode cell was used, with a carbon steel sample (working electrode), a large-area platinum wire (counter-electrode), and a saturated calomel electrode (reference electrode).

EIS measurements were performed using a sinusoidal wave with an amplitude of 10 mV and frequency range of 10^5 Hz to 10^{-1} Hz acquiring 8 measures per frequency decade, while PDP curves were obtained by polarizing carbon steel samples from -300 mV_{SCE} to $+700$ mV_{SCE} regarding the OCP, at a scan rate of 0.333 mV s⁻¹. At least two replicates were performed for each sample.

The considerably low scan rate is usually applied and presented in the adopted literature to clearly observe reactions stages^{17,18}. The inhibiting efficiencies obtained from EIS and polarization curves were calculated according to Equations 3 and 4, respectively.

$$IE_{EIS}(\%) = \left(\frac{R_{ctinh} - R_{ct0}}{R_{ctinh}} \right) \times 100 \quad (3)$$

$$E_{PDP}(\%) = \left(\frac{I_{corr} - I_{corrinh}}{I_{corr}} \right) \times 100 \quad (4)$$

The parameter R_{ct} stands for the charge transfer resistance, and I_{corr} the corrosion density current. The subscripts “inh”

and “0” refer to the presence and absence of the inhibitor, respectively. The values of R_{ct} were obtained from EIS electrochemical fitting, using the software Zview, while corrosion currents were obtained by Tafel extrapolation from the polarization curves, using the software NOVA 2.1.

2.5. Surface analysis – scanning electron microscopy and optical microscopy

Carbon steel surfaces analyzed by SEM (Hitachi TM 3030 Plus) were primarily submitted to corrosion tests, with and without corrosion inhibitors and the surfactant, rinsed with distilled water and acetone, dried, and conducted to surface morphology assessment.

Optical microscopy (Smartzoom 5, WEISS) was also performed on carbon steel surfaces after weight loss tests and chemical etching in order to obtain a macro visualization of the coupon and possible localized corrosion processes, such as pitting. The largest pits detected in each sample were analyzed by the Smartzoom built-in 3D surface reconstruction tool, enabling the determination of its depth and width. As previously mentioned, optical microscopy was also employed to obtain the exposed area of samples used in electrochemical tests.

2.6. Molecular modeling - computational details

Complete optimization of the SB1, SB2, and SB3 structure models in their neutral and acidic forms was performed based on the density functional theory (DFT) in the gas phase. Theoretical calculations were achieved using the B3LYP¹⁹

functional and the base function 6-31G(d,p) in the description of all atoms, implemented by the Gaussian 09 package²⁰. Electronic and quantum parameters, such as the energy of the busiest orbital (E_{HOMO}) and of the least vacant orbital (E_{LUMO}), band-gap energy, hardness and soft, Mulliken partial charges on the HOMO and LUMO orbitals were calculated based on the most stable neutral and protonated molecules.

3. Results

3.1. Characterization

3.1.1. FTIR

The FTIR spectra of the amines used as SBs precursors exhibited two characteristic bands for the N–H stretching at 3427 and 3353 cm^{-1} for aniline, 3445 and 3373 cm^{-1} for o-toluidine, and 3424 and 3348 cm^{-1} for 4-ethyl-aniline. The FTIR spectra of the inhibitors did not show the absorption bands referring to the functional groups N–H of the amines, indicating that they were absent after the reaction. Confirming SBs formation, the absorption band for the C=N stretch of imines was observed at 1662–1679 cm^{-1} . Imines exhibit an absorption band of varying intensity between 1690 and 1640 cm^{-1} , which is very close to the absorption range of the C=C bond^{11,15,21,22}.

The spectra also exhibit bands at 2983–2714, 2983–2815 and 2962–2813 cm^{-1} for SB1, SB2, and SB3, respectively, which are related to the C_{sp^3} –H stretch of aromatic rings. There are also bands at 807–838 cm^{-1} for angular deformation of C–H from 1,4-disubstituted aromatic ring phenol^{23,24}. In the spectra of SB2, there are also bands at 724 and 779 cm^{-1} related to C–H angular deformation from 1,2-disubstituted aromatic ring phenol²³. Moreover, bands at 1312 and 1362 cm^{-1} for SB1, 1316 and 1363 cm^{-1} for SB2, and 1314 and 1372 cm^{-1} for SB3 are related to C–N stretch of aromatic tertiary amine.

3.1.2. ¹H-NMR

The ¹H-NMR spectra showed intense doublets with chemical shifts (δ) in 3.04 and 3.07 ppm for inhibitors SB1 (Figure 3a), SB2 (Figure 3b), and 3.06 and 3.09 ppm for SB3

(Figure 3c), related to the hydrogens of the methyl groups ($-\text{N}(\text{CH}_3)_2$). Peaks between 6.68 and 7.80 ppm in all spectra refer to aromatic hydrogens, except for the singlet referring to CDCl_3 solvent deuterium in 7.27 ppm for SB3. The peaks at 8.31 ppm (SB1), 8.21 ppm (SB2) and 8.35 ppm (SB3) refer to the hydrogens of the iminic group ($\text{N}=\text{CH}$). These peaks confirm the formation of the Schiff bases from the condensation reactions^{11,15,22,25–27}. The chemical shift 2.34 ppm (SB2) refers to the methyl group hydrogens of o-toluidine. In addition, peaks at 1.25 ppm and between 2.35–2.72 ppm (SB3) refer to the ethyl group hydrogens of 4-ethyl-aniline.

3.1.3. Weight loss measurements

Gravimetric tests performed during 24 h in 1 M HCl yielded the corrosion rates (CR) and inhibition efficiency (IE_{WL}) values shown in Table 1. Efficiency values varying from 64.98% (SB3, 100 ppm, 333 K) to 92.28% (SB1, 600 ppm, 318 K) were obtained. Overall, the analysis of the SBs performances indicated a more significant reduction of corrosion rates and, consequently, improved efficiencies for SB1 and SB2. On the other hand, the lowest efficiency values were obtained for SB3. Regarding the concentration effect, results from Table 1 showed that its increase to 600 ppm provided higher efficiencies for all SBs, regardless of the temperature. Such tendency can be related to better coverage of the metallic surface by the existing amount of inhibiting molecules in the medium, preventing aggressive forms of corrosion^{28–30}.

Corrosion rates were also severely impacted by rising temperatures in the tests with and without the SBs. For the blank sample, enhanced corrosion can be related to the decrease of hydrogen evolution overpotential^{31,32}. In contrast, for samples in contact with corrosion inhibitors, increased corrosion rates can be related to desorption, decomposition, and rearrangement of inhibitory molecules, exposing the metallic surface and reducing the inhibition efficiency^{33,34}.

For better understanding and ease of comparison between results, the values from Table 1 were plotted in Figure 4. As seen for SB1, the temperature increase enhanced the concentration effect, since the differences in inhibition efficiencies between 100 ppm and 600 ppm were more significant at 318 K or

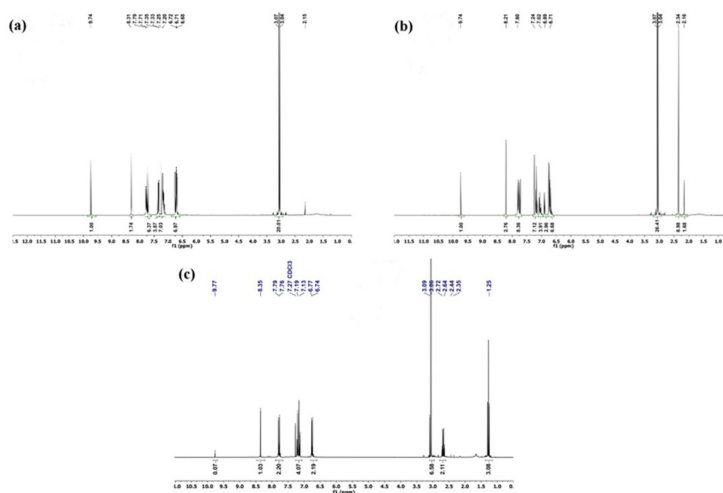
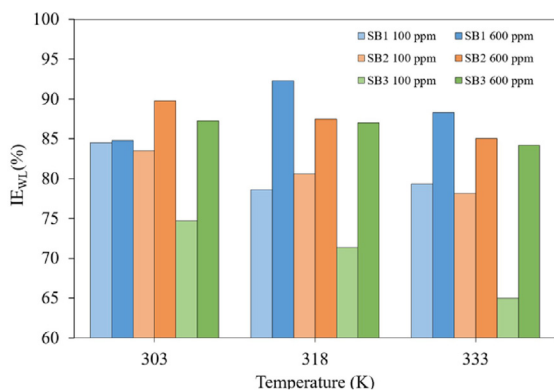


Figure 3. ¹H-NMR spectra of SB1 (a), SB2 (b), and SB3 (c).

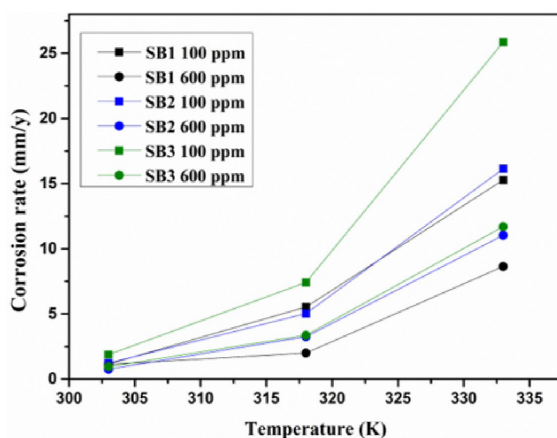
Table 1. Corrosion rates (mm/y) for API P-110 and inhibition efficiencies (%) using different concentrations of SB1, SB2, and SB3 in 1 M HCl.

Test	Concentration (ppm)	303 K		318 K		333 K	
		CR (mm/y)	IE _{wl} (%)	CR (mm/y)	IE _{wl} (%)	CR (mm/y)	IE _{wl} (%)
Blank	0	7.37 ± 0.53	-	25.90 ± 1.37	-	79.89 ± 1.67	-
SB1	100	1.14 ± 0.06	84.49	5.53 ± 0.15	78.63	15.28 ± 1.24	79.32
	600	1.12 ± 0.11	84.79	2.00 ± 0.19	92.28	8.65 ± 0.15	88.30
SB2	100	1.22 ± 0.16	83.48	5.03 ± 0.63	80.59	16.15 ± 0.95	78.14
	600	0.76 ± 0.03	89.73	3.25 ± 0.52	87.46	11.03 ± 0.31	85.07
SB3	100	1.87 ± 0.18	74.69	7.42 ± 0.36	71.36	25.87 ± 1.29	64.98
	600	0.94 ± 0.05	87.28	3.36 ± 0.26	87.01	11.70 ± 0.33	84.16

**Figure 4.** Inhibition efficiencies for API P 110 carbon steel after 24 h gravimetric tests in 1 M HCl in different concentrations of SB1, SB2, and SB3 from 303 to 333 K.

333 K than at 303 K. As a matter of fact, SB1 was the only base whose efficiency at 600 ppm increased when the temperature was raised to 318 K. This can be related to the conjugated effect of major molecules mobility with its greater concentrations at 318 K. On the other hand, at 333 K, the temperature has reached the limit to unbalance adsorption/desorption favoring the desorption of the inhibitor from the metallic surface, slightly decreasing the efficiency³⁵. The combined effect of temperature and concentration was not observed on the other bases (SB2 and SB3) whose efficiencies remained practically unchanged (600 ppm) or progressively decreased (100 ppm) with temperature.

Overall, the efficiencies of SB1 and SB2 were higher than those obtained for SB3, especially for the lowest concentration (100 ppm) and higher temperature (Figure 4). Given the differences in the molecular structures of the inhibitors, such as the methyl group from *o*-toluidine in SB2 ($-\text{CH}_3$), and an ethyl group from 4-ethylaniline in SB3 ($-\text{CH}_2\text{CH}_3$), a mobility reduction and the intensification of intermolecular steric effects are expected for these molecules as the substituent chain is increased. Some authors highlighted that the increase in the number of substituents might cause overcrowding, leading to the loss of molecule planarity and reduction in the interaction with the metallic surface. In addition, an increase in the degree of chain branching may also disturb the efficiency due to higher steric hindrance^{36,37}. Therefore, the lower efficiency of SB3 can be explained in terms of steric effects preventing efficient adsorption on the metallic surface.

**Figure 5.** Corrosion rates for API P 110 carbon steel after 24 h gravimetric tests in 1 M HCl under different concentrations of SB1, SB2, and SB3 from 303 to 333 K.

Trabanelli³⁸ analyzed the inhibitory effect of substituted compounds as a methyl group inserted in pyridine. It was found that the inhibitory effect increased when the electronic density was displaced towards the heteroatom of the chain. Thus, the closer is the methyl radical to the heteroatom, the greater the efficiency of the compound. The authors also studied the steric effect on the corrosion inhibitors performance for ferrous alloys. It was found that the lower the steric effect, i.e., the lower the substituting carbon chain, the greater its inhibition efficiency. In addition, when there is no difference in the steric impedance of the compounds, their efficiencies increase with the increase of the carbon chain. Therefore, Trabanelli's observations about the effects of substituting carbon chains on inhibitors are aligned with the results obtained for the inhibitory effect of SB1, SB2, and SB3.

The analysis of the corrosion rates in Figure 5 pointed out the similarities between samples immersed in SB1 100 ppm and SB2 100 ppm for all tested temperatures. However, it was noticed that, at 318 K and 333 K, increased concentrations (600 ppm) of SB1 performed better than SB2 due to steric effects. Regarding SB3, though the corrosion rates from samples immersed in SB3 600 ppm were very similar to SB2 600 ppm, its values under 100 ppm were the largest obtained. Such observation can be related to the more pronounced steric effect of the *p*-substituent radical, which is larger and further from the heteroatom. It was concluded, then, that the size limit of the carbonic radical that could be added to the SB1 aromatic ring, prevented from aniline, without reducing

the performance of the inhibitor, is 1 ($-\text{CH}_3$, methyl) since the ethyl substituent on SB3 provided higher CR values³⁹⁻⁴². Nevertheless, results revealed that all inhibitors were efficient and significantly reduced the corrosion rate of the alloy, and the values obtained are consistent with data observed in other studies in the literature, as indicated in Table 2.

In order to further reduce the corrosion rates, the best inhibitors (SB1 and SB2) were tested with the surfactants ethoxylated nonyl phenol (A1) and ethoxylated lauryl alcohol (A2). Assays were performed at the highest temperature (333 K) to evaluate a possible synergism in the most aggressive condition.

3.1.4. Surfactants effect

A surfactant is a surface active agent which can be used in corrosion inhibitory formulations due to two reasons: (i) improving the corrosion inhibitor miscibility in the acidic media enhances inhibitory performance, and (ii) the surfactant molecules can prevent corrosion due to the presence of electron rich groups, shown in Figure 6, motivating the analysis of its sole effect on corrosion protection⁴³. Thus, to assess higher efficiencies, formulations were developed based on SB1 and

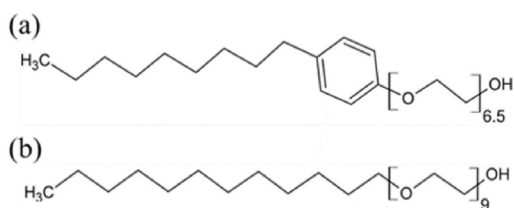


Figure 6. Molecular structure of (a) A1 and (b) A2 surfactants.

SB2 concentrations with the best outcomes (600 ppm) and an amount of surfactant corresponding to 2.5%wt. of the SBs concentration. Results for gravimetric tests performed in HCl 1 M at 333 K are shown in Table 3. It is important to point out that the overall concentration was still 600 ppm.

Results from Table 3 confirmed that the sole presence of the surfactants could inhibit corrosion even at concentrations as low as 15 ppm⁴³. Their comparison showed lower efficiency for A1 (67.61%) than A2 (81.46%). Such improved inhibitory effect of A2 was probably due to its greater hydrophilia compared to A1 (greater HLB), resulting in better miscibility in water, foaming power, wettability, and detergency.

However, A1 enhanced inhibition efficiencies better than A2 when combined with either of the inhibitors. This observation was confirmed by SB1 + A1 and SB2 + A1 corrosion rates, which were approximately 16% and 31% lower than SB1 + A2 and SB2 + A2, respectively. This behavior can be associated with the presence of the aromatic ring in A1, while A2 is aliphatic. In this sense, it is possible that the presence of the aromatic ring constitutes an important adsorption site through π - π interactions. It was observed that such trend prevailed over the hydrophilia of the surfactants.

Other studies in the literature investigated the synergistic effect of corrosion inhibitors and surfactants, reporting similar results. Zehra et al.⁴⁴ investigated a glycine derivate (100 ppm) as a corrosion inhibitor blended with 5 ppm with sodium dodecyl sulfate or cetyl pyridinium chloride in HCl 1 M, reaching efficiencies for potentiodynamic tests of 92.84% and 96.36%, respectively, while the sole analysis of the corrosion inhibitor yielded an efficiency of 88.64%.

Table 2. Inhibition efficiencies obtained for SB1, SB2, and SB3 compared to other Schiff bases from the literature as corrosion inhibitors in 1 M HCl.

Inhibitor/Concentration	IE(%)		Reference 323-333 K
	298 K	333 K	
SB1 / 600ppm	84.79	88.30	This work
SB2 / 600 ppm	89.73	85.07	
SB3 / 600 ppm	87.28	84.16	
B2 / 300 mg/L	96.50	85.90	35
PASP/SB / 80 mg/L	88.97	84.86	39
DMAHB / 5×10^{-3} M	87.30	89.92	40
BPT / 2.13 mmol/L	81.40	94.20	41
DBB / 5×10^{-4} M	85.69	92.60	42

Table 3. Corrosion rate (mm/y) and inhibition efficiency (%) for API P-110 in 1 M HCl in the presence of SB1 and SB2 isolated and blended with A1 and A2 at 333 K.

Compound (s)	Inhibitor concentration (ppm)	Surfactant concentration (ppm)	Total concentration (ppm)	Corrosion rate (mm/y)	Efficiency (%)	Synergism parameter (S)
A1	-	15	15	23.93 ± 1.33	67.61	-
A2	-	15	15	13.70 ± 2.11	81.46	-
SB1	600	-	600	8.65 ± 0.15	88.30	-
SB1 + A1	585	15	600	5.94 ± 1.10	91.97	1.70
SB1 + A2	585	15	600	7.10 ± 0.69	90.40	1.89
SB2	600	-	600	11.03 ± 0.31	85.07	-
SB2 + A1	585	15	600	5.17 ± 0.90	93.00	1.65
SB2 + A2	585	15	600	7.55 ± 0.61	89.78	1.86

The synergism parameter was calculated according to the relationship given by Aramaki and Hackerman that was reported elsewhere^{45,46}.

$$S = \frac{1 - (I_1 + I_2)}{1 - (I'_{1+2})} \quad (5)$$

Where, I_1 = inhibition efficiency of the SB; I_2 = inhibition efficiency of surfactant; I'_{1+2} = measured inhibition efficiency for the combined formulation SB+surfactant. When S approaches 1 no interaction between the inhibitor compounds is observed, while $S > 1$ indicates that a synergistic effect occurred. When $S < 1$, the antagonistic interaction of the selected compounds prevailed, which could be attributed to a competition to adsorb over the surface. Since the observed values were 1.70 (SB1+A1), 1.89 (SB1+A2), 1.65 (SB2+A1), and 1.86 (SB2+A2) the synergistic effect was observed for all formulations.

3.1.5. Thermodynamic parameters

The Arrhenius equation (Equation 6) correlates the uniform corrosion rate to the apparent activation energy of dissolution in carbon steel (E_a), where R is the universal constant of ideal gases (8.314 J/mol K), T is the absolute temperature, and A is the pre-exponential factor.

$$\log CR = \frac{-E_a}{2.303RT} + \log A \quad (6)$$

The apparent activation energies of dissolution in carbon steel (E_a) were obtained for each SB from linear adjustments of the data (Table 4 and Figure 7). All the obtained quadratic regression coefficients (R^2) were above 0.92, which indicated that the Arrhenius kinetic model could precisely describe the corrosion mechanism.

The activation energies (E_a) in the absence and presence of corrosion inhibitors provide information about the inhibitory mechanism. Previous studies in the literature^{33,47-49} related chemical and physical adsorption to temperature effects. The E_a values in the absence of inhibitors are reference values to the inhibited systems. When efficiency decreases with the increase of temperature, the E_a value is higher in the presence of the inhibitors, indicating a coulombic type of adsorption, or physical adsorption. Chemical adsorption is observed when efficiency increases with temperature, and E_a is lower in the presence of the inhibitors. The value obtained for the activation energy of API P110 steel in 1 M HCl, in the absence of corrosion inhibitors, was 64.51 kJ/mol, which is in good agreement with previous studies in the literature⁵⁰⁻⁵³.

All values of apparent activation energy for the SBs at 100 ppm were greater than the E_a value of the blank sample and very close to each other, which indicated that the adsorption mechanism can be characterized by physisorption at 100 ppm. However, when the concentration is increased to 600 ppm, the E_a value for SB1 becomes lower than the blank, inferring the chemisorption mechanism. This observation agrees with the efficiency increase of SB1 at 600 ppm from 303 K to 318 K. This behavior was not observed for SB2 and SB3, whose E_a value remained above the blank test.

Table 4. Activation energies for API P110 carbon steel in 1 M HCl in the absence and presence of corrosion inhibitors.

Test	Concentration (ppm)	E_a (kJ mol ⁻¹)	R^2
Blank	0	64.51	0.9994
SB1	100	72.78	0.9906
	600	56.72	0.9279
SB2	100	72.37	0.9992
	600	74.98	0.9995
SB3	100	73.56	0.9999
	600	70.58	0.9996

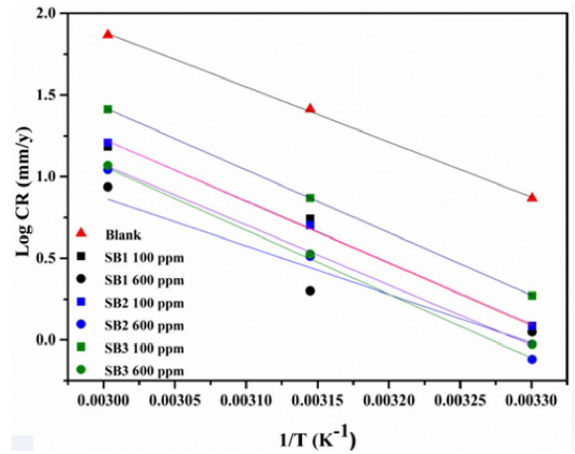


Figure 7. Arrhenius plots for API P110 carbon steel in 1 M HCl in the absence and presence of the inhibitors.

3.1.6. Adsorption isotherms

Adsorption models provide relevant information about the interaction between inhibitor molecules and the metallic surface³³. The process of molecules adsorption onto the metallic substrate is characterized by a substitution mechanism, where water molecules adsorbed on the metallic surface are replaced by inhibitory molecules. The relationship between the surface coverage (θ) and the inhibitor concentration (C) is used in the isothermal adsorption model⁵⁴. The tested models were Langmuir (Equation 7), Temkin (Equation 8), El-Awady (Equation 9), and Freundlich (Equation 10)^{55,56}:

$$\frac{C}{\theta} = \frac{1}{K_{ads}} + C \quad (7)$$

$$\theta = \left(\frac{-2.303}{2a} \right) \log K + \left(\frac{-2.303}{2a} \right) \log C \quad (8)$$

$$\log \frac{\theta}{1-\theta} = \log K + y \log C \quad (9)$$

$$\ln(\theta) = \ln(K_{ads}) + \ln(C) \quad (10)$$

K_{ads} is the adsorption equilibrium constant, $K_{ads} = K^{1/y}$, where y represents the number of inhibitory molecules occupying a given site, C stands for the inhibitor concentration, and θ is the fraction of the surface covered by the inhibitor.

Figure 8 illustrates the Langmuir isotherms data plot for the three inhibitors at 318 K. Table 5 presents the values of K_{ads} , the slopes, and the quadratic regression coefficients obtained.

The Langmuir model best represented the results for all inhibitors. According to it, the adsorption of the molecules is characterized by a coating of an inhibitor monolayer on the metallic surface, with sites of the same energy level and electronic affinity, and the adsorbed molecules adjacent are supposedly free from steric effects and lateral interactions⁵⁷. Higher values of K_{ads} indicate better interaction between the inhibitor and the metallic surface. However, low values of K_{ads} indicate that interactions are weak, and consequently, adsorbed species can be easily removed by solvent molecules^{31,58}. SB1 and SB3 showed similar adsorption constants, while for SB2 the constant is almost three-fold of SB1 K_{ads} value. This may indicate that the slight activation of the SB2 aromatic ring caused by the methyl substituent may have favored adsorption. Besides showing higher K_{ads} values and, consequently, stronger adsorption to the metallic surface, the corrosion rates of SB2 were higher than SB1. This indicates that SB2 exhibited a stronger interaction with the metal, but not the best surface coverage due to steric effects. For SB3, the increase in K_{ads} value compared to SB1 was very small, indicating that the steric effects and greater distance from the substituent radical (ethyl) of the heteroatom in SB3 negatively affected its adsorption kinetics.

3.2. Electrochemical tests

3.2.1. Electrochemical impedance spectroscopy

EIS is an efficient method to study the corrosion phenomenon at the metal-solution interface. Nyquist and Bode plots for API P110 carbon steel in 1 M HCl in the presence and absence of the

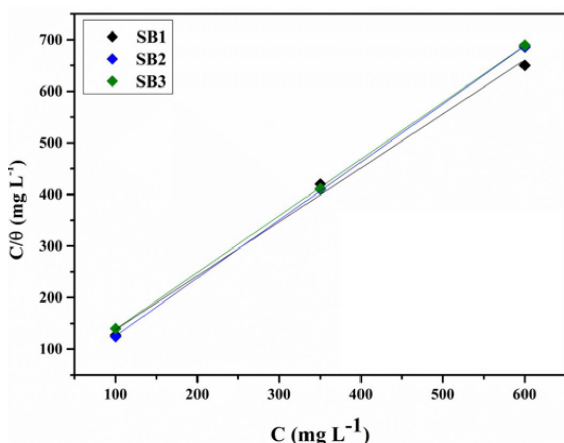


Figure 8. Langmuir adsorption isotherm model for API P110 carbon steel in 1 M HCl containing SB1, SB2, and SB3 at 318 K.

different concentrations of SBs and their combination with the surfactant A2 are shown in Figure 9 and Figure 10, respectively. Concerning the effect with surfactants, it should be highlighted that only A2 was investigated in the electrochemical tests since it has greater hydrophilicity and consequently resulting in better miscibility in water than A1. In addition, nonyl phenol surfactants have been replaced due to their toxicity. A2 is a nonionic surfactant resulting from the reaction of fatty acids obtained from vegetable oil that makes this surfactant a better option. The Nyquist plots show depressed semicircles, capacitive-like at high and intermediate frequency values (Figure 9a). Since Bode diagrams disclosed only one time constant during the corrosion phenomenon, the steel corrosion is mainly under charge transfer control. A small dispersion at lower frequencies could be identified, especially for samples immersed in solutions containing SBs, which can be related to the heterogeneity of the adsorbed film⁵⁹. The plots show similar shapes when comparing the blank and SB1 100 ppm, which indicates that the corrosion mechanism shows no significant change in the presence of inhibitor at this concentration.

Similarly to gravimetric tests, impedance results clearly showed the influence of the SB concentration on the corrosion process, yielding greater capacitive arcs and impedance modules for greater concentrations of both SB1 and SB2, indicating better corrosion protection in HCl 1 M. The concentration effect can also be pointed out by the greater phase angle peaks displayed by both SBs at 600 ppm and the fact that such peaks are shifted to higher frequencies, when compared SBs at 100 ppm and the blank sample. The comparison between SB1 and SB2 performances under 600 ppm showed improved corrosion protection for SB1, since impedance modulus on low frequencies (0.1 Hz) of 57.19 Ohm.cm² and 32.62 Ohm.cm² could be identified in Figure 10 for SB1 and SB2, respectively.

The difference between the synergetic behavior displayed by samples SB1+A2 and SB2+A2 becomes clearer when analyzing the shape of the phase angle peak displayed by the latter, which seems to be formed by the merge of two other peaks under high frequencies, while the sample SB1 + A2 displayed a single peak with shape similar to samples without the addition of A2. Such differences may be associated with two or more reaction steps occurring on the metallic surface, probably associated with the adsorption mechanism of the inhibiting molecules and the surfactant.

Randles circuit (Figure 11) was employed to fit EIS results, using the software Zview. The parameters within the model are: electrolyte resistance (R_s), charge transfer resistance (R_{ct}), and the constant phase element, which models the non-ideal behavior of the double layer, as described in Equation 11. The constant Y_0 is analogous to the capacitance, while the parameter n indicates different physical phenomena, including surface roughness, inhibitor adsorption and/or desorption.

Table 5. Adsorption parameters calculated from Langmuir, Temkin, El-Awady, and Freundlich adsorption isotherms.

Inhibitor	Langmuir			Temkin		El Awady		Freundlich	
	K_{ads} (L mg ⁻¹)	R ²	Slope	R ²	Slope	R ²	Slope	R ²	Slope
SB1	0.0302	0.9976	1.0460	0.8443	0.0693	0.7721	0.5846	0.8589	0.0817
SB2	0.0752	0.9999	1.1238	0.9999	0.0384	0.9981	0.2869	0.9999	0.0458
SB3	0.0353	0.9999	1.1002	0.9658	0.0894	0.9782	0.5622	0.9622	0.1132

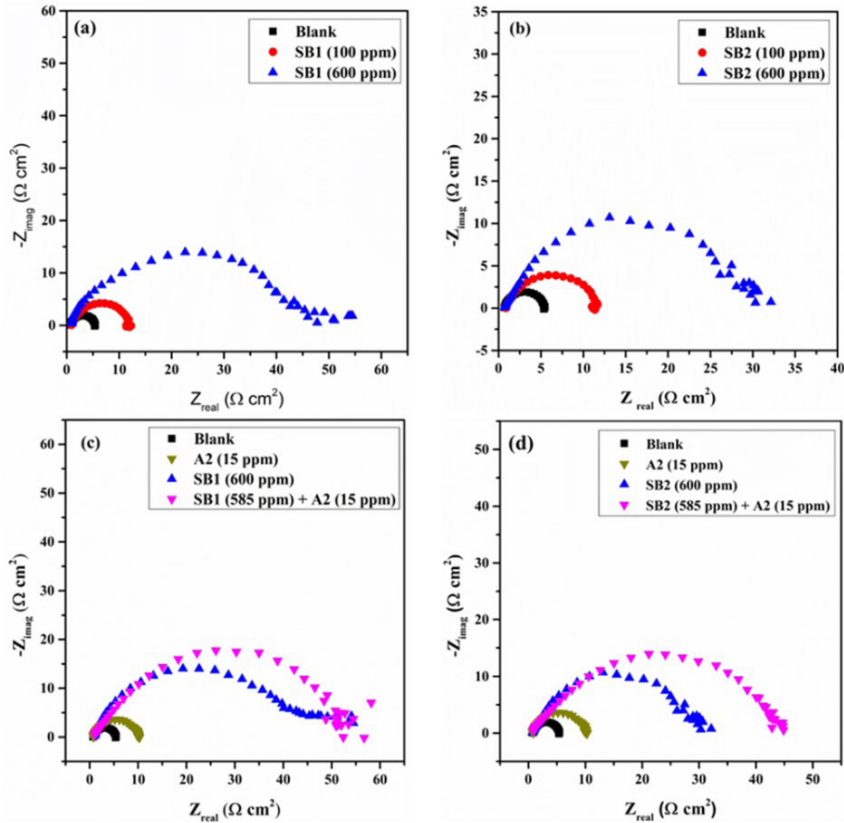


Figure 9. Nyquist plots for carbon steel API P110 at 333 K in 1 M HCl for the concentration effect of SB1 (a), concentration effect of SB2 (b), surfactant A2 with SB1 (c), surfactant A2 with SB2 (d).

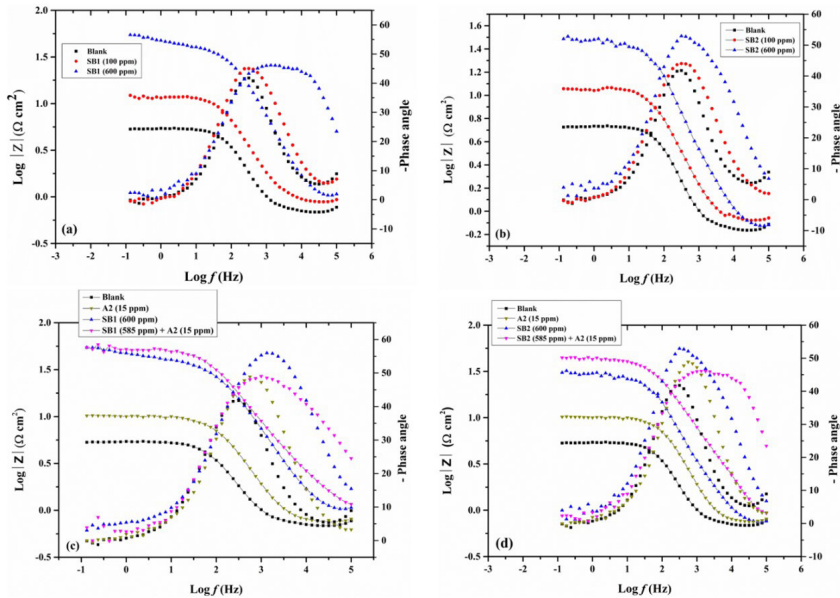


Figure 10. Bode plots for carbon steel API P110 at 333 K in 1 M HCl for the concentration effect of SB1 (a), concentration effect of SB2 (b), surfactant A2 with SB1 (c), surfactant A2 with SB2 (d).

Thus, when n is equal to 1, Equation 11 corresponds to an ideal capacitor, while $0.5 < n < 1$, Equation 11 takes into account the non-ideal behaviors of the double layer, flattening the capacitive arcs in Nyquist diagrams. This parameter also

indicates the heterogeneity of the inhibiting film when this value moves away from 1. Fitting results, listed in Table 6, presented chi-squared values ranging from 4.0×10^4 to 9.8×10^{-3} , indicating good fitting to the equivalent circuit.

Table 6. Parameters obtained by EIS for corrosion of API P110 carbon steel in 1 M HCl without and with different concentrations of SB1, and the surfactant effect at 333 K.

Sample	R_s (Ohm.cm ²)	R_{ct} (Ohm.cm ²)	Y_0 (CPE) (S ⁿ .Ω ⁻¹ .cm ²)	n (0< n <1)	IE (%)
Blank	0.787±0.129	5.360±0.909	7.93x10 ⁻⁴ ±1.53x10 ⁻⁴	0.866±0.003	-
SB1 (100 ppm)	0.922±0.074	10.200±1.302	6.41x10 ⁻⁴ ±2.45x10 ⁻⁵	0.804±0.001	47.45
SB1 (600 ppm)	0.888±0.325	35.990±7.269	1.53x10 ⁻⁴ ±4.24x10 ⁻⁶	0.766±0.016	85.11
SB2 (100 ppm)	0.833±0.020	8.593±3.007	8.19x10 ⁻⁴ ±1.42x10 ⁻⁴	0.791±0.017	37.63
SB2 (600 ppm)	0.911±0.067	34.075±5.678	4.59x10 ⁻⁴ ±2.89x10 ⁻⁵	0.727±0.030	84.27
A2 (15 ppm)	0.744±0.009	8.713±0.982	3.80x10 ⁻⁴ ±1.77x10 ⁻⁵	0.851±0.000	38.48
SB1 (585 ppm) + A2 (15 ppm)	0.886±0.002	57.420±3.620	2.80x10 ⁻⁴ ±2.47x10 ⁻⁵	0.681±0.002	90.67
SB2 (585 ppm) + A2 (15 ppm)	0.733±0.218	48.145±4.009	3.36x10 ⁻⁴ ±9.55x10 ⁻⁵	0.671±0.034	88.89

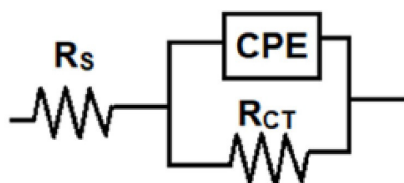


Figure 11. Equivalent circuit used to fit EIS obtained for API P110 carbon steel in 1 M HCl.

$$Z_{CPE} = \frac{1}{Y_0(j\omega)^n} \quad (11)$$

According to Table 6, all solutions presented low resistance, despite the addition of organic molecules in the medium. Thus, the ohmic drop was not an issue. Regarding the charge transfer resistance, fitting results provided increasing R_{ct} values with SBs addition, confirming the inhibitory adsorption layer on the metallic surface, protection against the corrosive process, as also pointed out by the gravimetric and polarization results. Furthermore, there was no significant difference between both bases performances when compared under the same concentrations (100 or 600 ppm). However, when SBs were combined with the surfactant A2, there was an expressive increase of R_{ct} to 57.42 ± 3.62 and 48.15 ± 4.00 , for samples SB1 + A2 and SB2 + A2, respectively. Such result could be visually perceived during immersion (OCP measurement), since hydrogen evolution was less vigorous for samples combining the SB and surfactant. Nevertheless, it is important to highlight that, differently from the gravimetric and polarization tests, EIS results presented a significant difference between samples SB1 + A2 and SB2 + A2, where the former presents the greatest R_{ct} of all samples.

Table 6 also describes a tendency of Y_0 reduction with increasing SBs concentrations. According to Equation 11, the smaller the Y_0 , the greater Z_{CPE} and, consequently, the smaller the tendency to accumulate charges on the double layer. The addition of an inhibitor to an electrochemical system promotes the displacement of water molecules initially adsorbed to the metal surface, leading to the adsorption of inhibitory molecules. This phenomenon alters the metal-solution interface, modifying the electrical double layer. The adsorption of the inhibitor occurs because the energy of interaction between the metal and the inhibitor is greater than between the metal and water molecules⁶⁰. Thus, in the present context, the reduction of Y_0 is related to the adsorption of organic molecules to the metal surface. The

reduced values of n for increased concentrations of SBs also corroborate such results, since the obtained results are shifted from the value of an ideal electric double layer ($n = 1$). This reduction of n is related to the increase of the surface heterogeneity, caused by the greater inhibitor coverage at higher concentrations. When $\alpha = 1$, the Y_0 is identical to an ideal capacitor, indicating the metal/solution interface is capacitive in nature. Furthermore, the Y_0 value reveals the characteristics of the metal surface film. The lower Y_0 value for systems with a higher amount of inhibitor or in the presence of A2 indicates a denser inhibiting film⁶¹. Attention can be drawn to samples SB1 + A2 and SB2 + A2, whose n values were the lowest of all samples.

By the analysis of the efficiencies, it was observed that, both SB1 and SB2 exhibited very similar efficiencies (85.11% for SB1 and 84.27% for SB2), which corroborates the gravimetric and previous electrochemical data. When combining the SBs with surfactant (A2), the efficiency values of SB1 and SB2 increased to 90.76% and 88.89%.

3.2.2 Potentiodynamic polarization

In this study, the Tafel extrapolation method was applied to the polarization curves presented in Figure 12 to obtain the electrochemical parameters shown in Table 7, including corrosion current density (I_{corr}), corrosion potential (E_{corr}), cathodic and anodic Tafel slopes (β_c and β_a). To accurately use Tafel extrapolation, the considered interval should be at least 50-100 mV away from the corrosion potential and at least one of the branches should exhibit linearity behavior on the semilogarithmic scale over minimum of one decade of current density⁶². The presence of an inflection in the anodic branch provided a poorly defined experimental anodic Tafel region, which precludes accurate evaluation of the anodic Tafel slopes (β_a) by Tafel extrapolation. However, observations could be performed based on I_{corr} and E_{corr} displacement, as well as cathodic branches⁶³.

According to the results, SB1 showed an I_{corr} reduction of 80.76% and 93.48% when in concentrations of 100 and 600 ppm, respectively, while SB2 promoted I_{corr} reductions of 80.43% and 81.58% for 100 ppm and 600 ppm, respectively, corroborating the weight loss measurements. Besides, both anodic and cathodic branches were affected by the presence of the inhibitor, where more pronounced effects could be perceived under the highest concentration (Figure 12). This modification of the branches can be numerically identified by the value of β_c in Table 7, which is much larger for 600 ppm than 100 ppm.

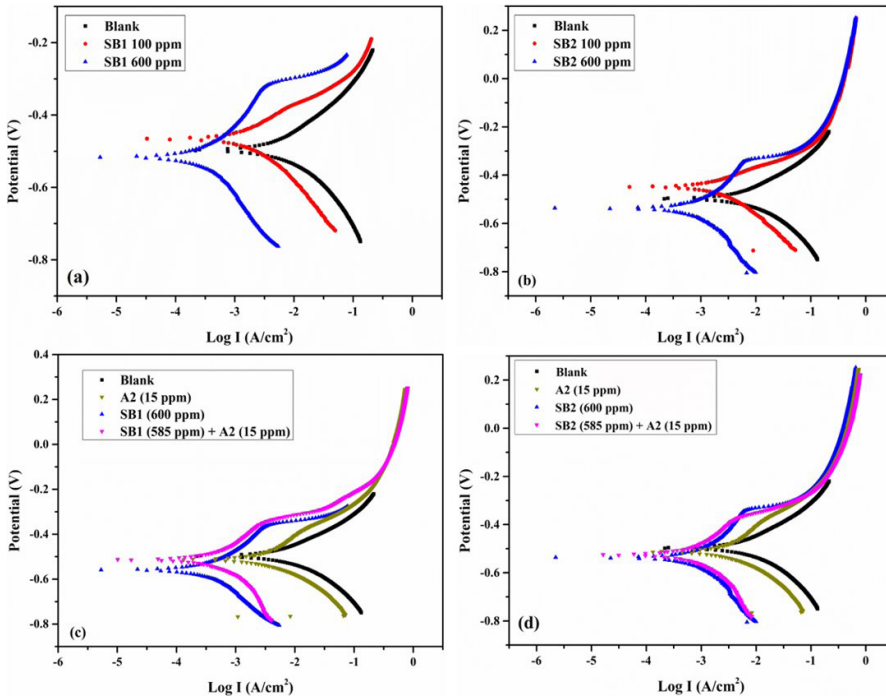


Figure 12. PDP plots for carbon steel API P110 at 333 K in 1 M HCl for the concentration effect of SB1 (a), concentration effect of SB2 (b), surfactant A2 with SB1 (c), surfactant A2 with SB2 (d).

Table 7. Parameters obtained by PDP for corrosion of API P110 carbon steel in 1 M HCl without and with different concentrations of SB1, and the surfactant effect at 333 K.

Sample	$-E_{\text{corr}}$ (mV)	I_{corr} (mA/cm ²)	β_c (mV/dec)	β_a (mV/dec)	IE_{PDP} (%)
Blank	497.68	6.08	149.52	139.06	-
SB1 (100 ppm)	466.72	1.17	122.60	-	80.76
SB1 (600 ppm)	558.91	0.39	216.40	-	93.48
SB2 (100 ppm)	449.00	1.19	109.71	-	80.43
SB2 (600 ppm)	543.04	1.12	291.80	-	81.50
A2 (15 ppm)	517.94	2.75	115.60	-	54.66
SB1 (585 ppm) + A2 (15 ppm)	500.44	0.49	189.31	-	91.81
SB2 (585 ppm) + A2 (15 ppm)	499.66	0.80	201.77	-	86.76

The inhibitor effect on the anodic branch shape indicated that the organic molecules interacted with the anodic sites, preventing iron dissolution. The iron cations formed during the anodic dissolution of carbon steel may form a complex with the inhibitory molecules, adsorbing onto the metallic surface. Additionally, the chloride ions adsorb onto the positively charged metallic surface through electrostatic interactions, followed by the adsorption of protonated organic compounds, which can either adsorb onto negative sites of the metallic surface or through electrostatic interactions with the pre-adsorbed chlorine ions⁶⁴. Therefore, SB1 molecules may get protonated and adsorb on anodic sites. Besides, this process might involve at least two different steps associated with the anodic branch inflections. The cathodic branch is also modified due to the inhibition of cathodic reactions. Some functional groups in SB1 structure may react with iron species, such as Fe^{2+} and Fe^{3+} , forming complexes that adsorb onto the metallic surface. This inhibition mechanism has been widely reported in other studies^{6,65-67}. Furthermore,

the corrosion potentials in the presence of both SBs, regardless of the concentration, provided differences regarding the blank sample smaller than 85 mV, confirming that the inhibitors adsorbed both on anodic and cathodic sites^{68,69}.

It is important to mention that the anodic branches, especially for samples SB1 600 ppm, SB2 600 ppm, SB1/A2 and SB2/A2, exhibited two regions with different rates of current variation. Such rates can be influenced at some level by (i) diffusion processes caused by the adsorbed organic film, and its heterogeneity, especially for the region with lower current variation rates, and (ii) the formation of complexes yielding different anodic reactions with different velocities. EIS results corroborate a possible influence of the diffusion mechanism and surface heterogeneity under higher SB concentrations since the n value also decreased for such samples.

From the tests with SB2 and A2, it could be observed that E_{corr} and β_c from A2 are closer to the blank sample. SB2 (600 ppm) shows the highest difference of β_c when compared

to the blank system, which is related to the adsorption of inhibiting species on the cathodic sites. However, SB2 + A2 sample provided values closer to the blank sample. This observation indicates a possible modification in the adsorption of molecules to the metallic surface. It might be associated with (i) the A2 aid so SB2 molecules can adsorb more easily, (ii) complexes formation between A2 and SB2 molecules, (iii) the adsorption of A2 molecules where SB2 could not lead to a continuous film, or (iv) A2 molecules may form a second layer on the metallic surface, leading to a hindrance to the acidic solution. Besides, it can be observed from Figure 12c that A2 shows a lower inflection than SB2, while SB2 + A2 shows an inflection a little lower than SB2 due to the presence of A2, confirming its influence on the system. For the test between SB1 and A2, the efficiencies are a little lower than SB1 alone, which can be related to inhibitor desorption between the EIS and PDP tests, and modification of the electrode surface chemistry.

3.3. Surface characterization

3.3.1. Scanning electron microscopy

Figure 13 presents coupons scanning electron microscopies after 24 h immersion in 1 M HCl, considering the absence and presence of different inhibitor formulations, at 333 K and pickling. It can be seen in Figure 13a that the blank coupon surface presented high irregularity due to the corrosive attack. In addition, the test with A2 also revealed an irregular surface, which confirmed that the surfactant presented a minor influence on the corrosive process inhibition and was not the leading active agent. The tests with SB1 and SB2 revealed a more homogeneous surface, confirming the protection observed in the weight loss and electrochemical measurements. However, despite the lower corrosion rates presented by gravimetric and electrochemical tests, sample surfaces from SB1+A2 or SB2+A2 appeared more irregular

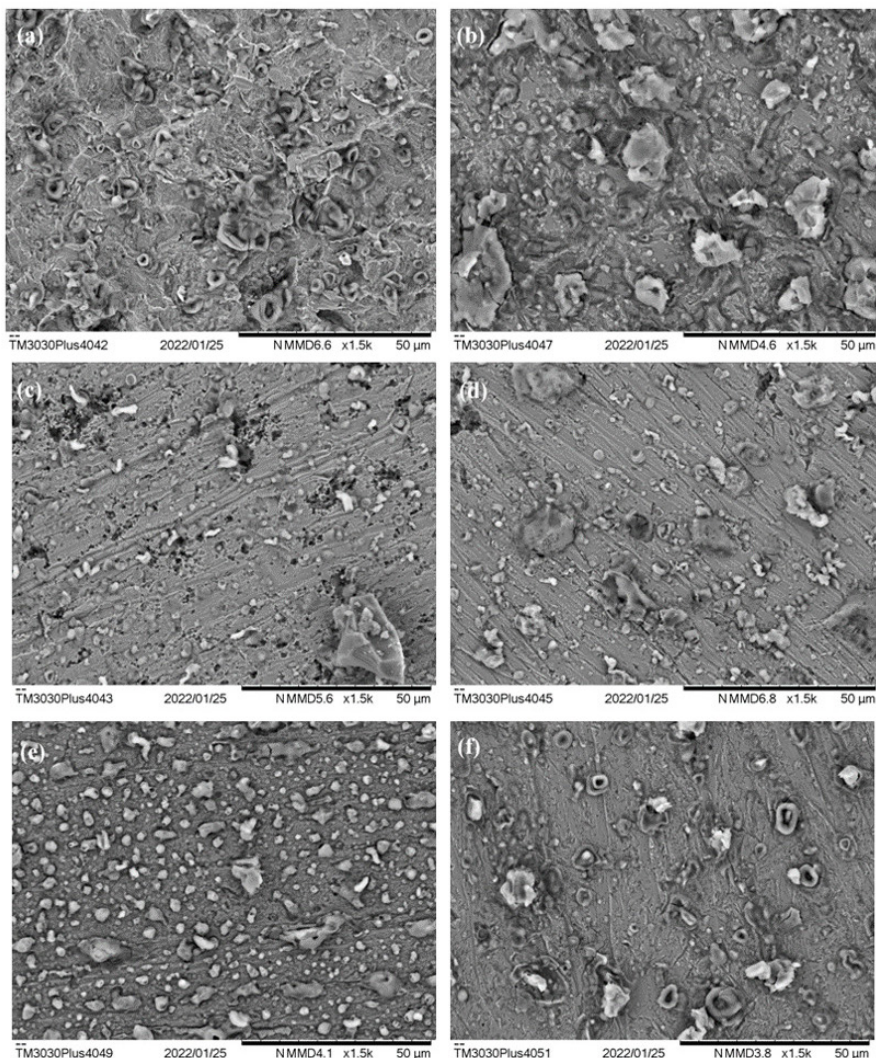


Figure 13. Scanning electron microscopy of API P 110 coupons after weight loss measurements in 1 M HCl at 333 K: (a) blank; (b) A2; (c) SB1; (d) SB2; (e) SB1 + A2; and (f) SB2 + A2.

than those immersed in SB1 or SB2 alone, indicating the presence of deposits other than corrosion products.

3.3.2. Optical microscopy

Optical microscopy was performed on the specimens after weight loss measurements at 333K in order to evaluate pit depth⁷⁰, according to ASTM G 46. The selected pits were measured, and the deepest pit identified in the sample is described in Table 8. According to the latter, no pits were detected on the blank and A2 samples, only uniform attack on the metallic surface. However, when samples are immersed in HCl solution containing SB1 or SB2, pits as deep as 111.30 μm and 228.40 μm , respectively, appeared, confirming that SB2 shows lower inhibition efficiency than SB1 for both uniform (as observed in weight loss tests) and localized corrosion.

The weight loss measurements showed a negligible synergism between SB1 and A2. However, when localized corrosion was evaluated, it indicated that A2 actually provides a harmful interference in the adsorption of SB1 in certain areas, leading to localized corrosion. It indicates that the adsorption mechanism has been modified. On the other hand, when SB2 was combined with A2, no localized corrosion was identified, even though steel samples immersed only in SB2 presented the deepest pits. Thus, the positive synergetic behavior identified in gravimetric and electrochemical tests for samples SB2+A2 could be extended to localized corrosion. As highlighted in section 3.2.1, SB1 is the only SB that showed two adsorption mechanisms (physisorption and chemisorption). Although A2 has favored the physisorption of SB2 to the metallic surface, the surfactant has probably interfered with the chemisorption of SB1, which explains the results in Table 8.

A possible explanation for the different behaviors exhibited by samples SB2 and SB2+A2 regarding localized corrosion is that SB2 alone led to possible uncovered areas, resulting in severe localized corrosion. These uncovered areas were probably related to the presence of a methyl substituent in the aromatic ring, making the uniform adsorption more difficult. However, when combined, A2 helps SB2 to adsorb on the metallic surface, as well as A2 molecules can also adsorb on the substrate. In that sense, SB2+A2 provided the best inhibitive results since it was able to prevent both uniform and localized corrosion efficiently.

3.4. Computational study

For the theoretical studies, three models were proposed for SB1, SB2, and SB3, shown in Figure 14, from top to

Table 8. Pitting depth of API P 110 coupons after weight loss measurements in 1 M HCl at 333 K: blank, A2, SB1, SB2, SB1 + A2 and SB2 + A2.

Tests	Pitting depth (μm)
Blank	-
A2	-
SB1	111.30
SB2	228.40
SB1 + A2	203.70
SB2 + A2	-

bottom. Structural, electronic, and quantum properties of these molecules were analyzed using calculations based on density functional theory (DFT). Fully optimized neutral phase compounds, shown vertically and horizontally (Figure 14a, b), demonstrated that the structures were not planar, with inclination relative to the two aromatic rings of the structure ranging from 141° to 145°, and with a value of 180° for a fully planar molecule.

When looking at inhibitors SB2 and SB3 that have bulky substituents, ortho-methyl group of inhibitor SB2 remained aligned with the substituted aromatic ring. However, in the case of inhibitor SB3, para-ethyl group remained perpendicular to the aromatic ring, indicating that the substituent may hinder the adsorption of the inhibitor onto the metallic surface, limiting adsorption through only one aromatic ring.

For all SBs, the HOMO and LUMO orbitals are mostly of π -type in the aromatic rings and σ -type in the tertiary amines. Besides, SB3 shows σ -type orbitals also in the para-ethyl substituent (Figure 14c, d). These results indicate that, for inhibitors SB1 and SB2, adsorption to the metallic surface probably occurs by one of the aromatic rings. However, for SB3, the presence of electron density in the para-ethyl group may lead to inefficient adsorption.

Quantum parameters, such as the energies of the highest occupied molecular orbital (E_{HOMO}), the lowest vacant molecular orbital (E_{LUMO}), the energy gap (ΔE) between E_{HOMO} and E_{LUMO} , dipole moment (μ), the overall electronegativity (χ), the hardness (η) and the softness (σ), were obtained using the optimized structure corresponding. Table 9 shows the quantum parameters for SB1, SB2, and SB3 in the neutral phase. The energy of the highest occupied molecular orbital indicates the tendency of a molecule to donate its electron density to electron acceptor compounds with empty molecular orbitals, such as metallic materials. Thus, high E_{HOMO} values indicate the tendency to adsorb on metallic surfaces, increasing the corrosion inhibition efficiency. Low bandgap values and increased dipole moment also enhance the ability of a molecule to act as a corrosion inhibitor. From the HOMO and LUMO orbital values from the molecules herein studied, it was possible to obtain the overall electronegativity, hardness, and softness, according to Equations 12-14.

$$\chi = -\frac{E_{\text{HOMO}} + E_{\text{LUMO}}}{2} \quad (12)$$

$$\eta = \frac{E_{\text{LUMO}} - E_{\text{HOMO}}}{2} \quad (13)$$

$$\sigma = \frac{1}{\eta} \quad (14)$$

Analyzing the results obtained for the SB1, SB2, and SB3 in the neutral phase, it was possible to notice that similar quantum properties were obtained for the three molecules, which were also similar to other inhibitors reported in the literature^{63,71}. A noteworthy difference was only observed in the SB2 dipole moment, which showed more promising values. This phenomenon indicated that the variation of the anticorrosion properties for SB1, SB2, and SB3 was more influenced by structural than electronic aspects.

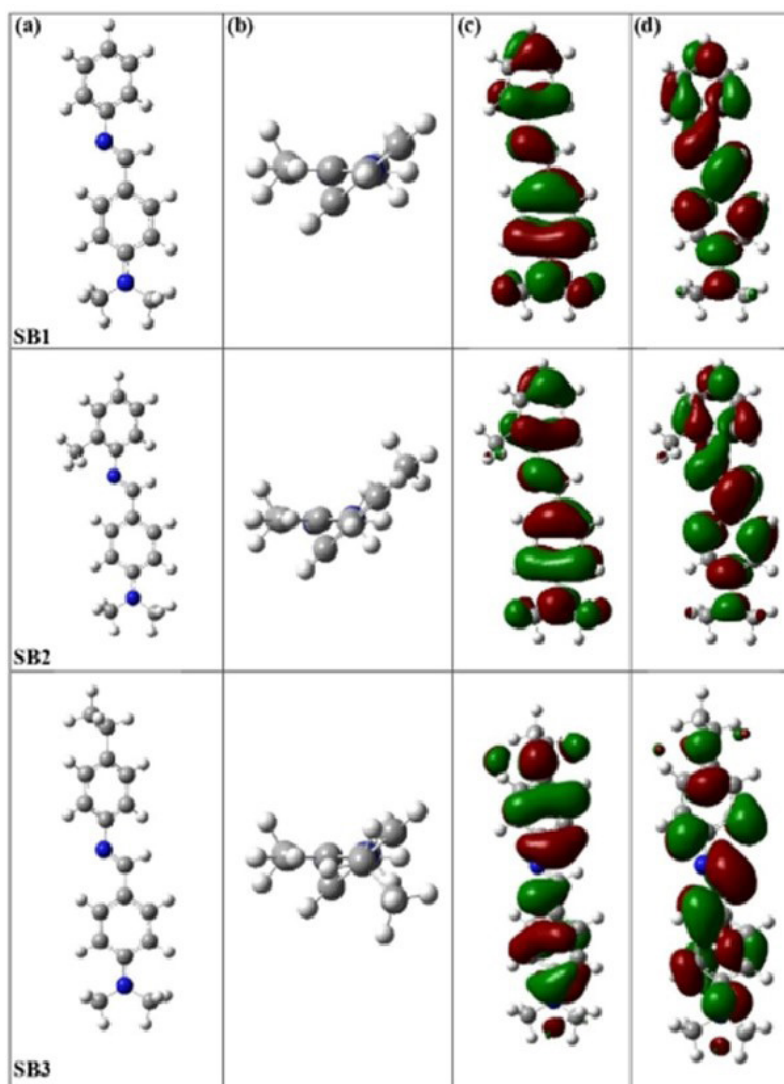


Figure 14. (a) Vertical and (b) horizontal view of the optimized structures of the SB1, SB2, and SB3 molecules in the neutral phase; (c) the highest occupied molecular orbital and (d) the lowest unoccupied molecular orbital. Colors of atoms are gray = carbon, blue = nitrogen, and white = hydrogen.

Table 9. Quantum parameters for SB1, SB2, SB3 and other organic molecules from literature in neutral state.

Quantum properties	E_{HOMO} (eV)	E_{LUMO} (eV)	ΔE (eV)	μ (D)	X (eV)	η (eV)	σ (eV ⁻¹)	Reference
SB1	-5.09	-1.10	3.99	4.55	3.09	2.00	0.50	-
SB2	-5.07	-1.08	3.99	4.76	3.07	2.00	0.50	-
SB3	-5.02	-1.06	3.96	4.15	3.04	1.98	0.51	-
<i>Peumus boldus</i>	-5.28	-0.52	4.76	2.33	2.90	2.38	0.42	⁶³
Schiff Base*	-5.25	-1.42	3.82	2.93	3.34	1.91	0.52	⁷¹

*2-methoxy-4-(((2-(methylthio)phenyl)imino)methyl)phenol

Besides the neutral phase, the structural, electronic and quantum properties from the SBs were also calculated in acidic medium, modeling the protonation of the structural heteroatoms (imine group and tertiary amine present in all three inhibitors). The ability of the inhibitors to be protonated in an acid medium was measured by Equation 15:

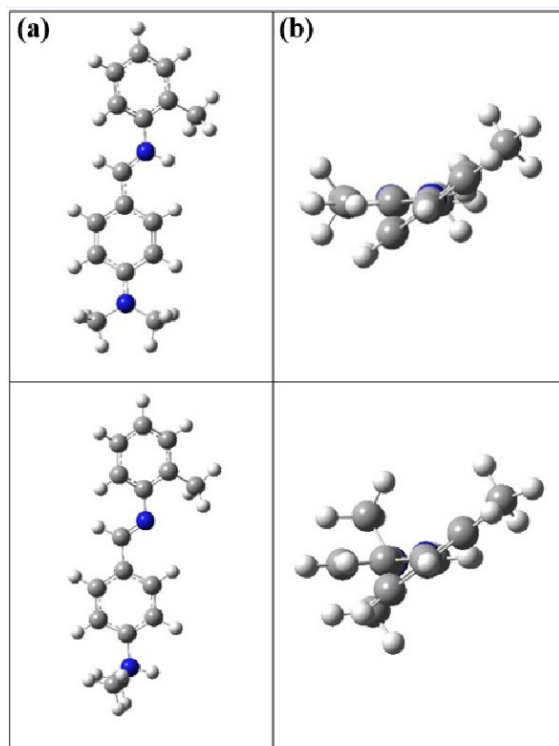
$$\Delta E_{\text{Prot}} = E_{\text{inhibitor}^+} - E_{\text{inhibitor}} \quad (15)$$

Where ΔE_{prot} stands for the protonation energy, $E_{\text{Inhibitor}^+}$ the energy of the protonated inhibitor molecule, and $E_{\text{Inhibitor}}$ is the energy of the inhibitor molecules in the neutral phase. The protonation energy of the inhibitors in their different heteroatoms is shown in Table 10.

For the two protonation possibilities within the SBs molecules, all H^+ remained in the structure. Even though there was no cracking or decomposition of the molecules,

Table 10. Quantum parameters of protonated inhibitors (SB1, SB2 and SB3) in different heteroatoms in the gas phase.

Quantum properties	E_{HOMO} (eV)	E_{LUMO} (eV)	ΔE (eV)	μ (D)	X (eV)	η (eV)	σ (eV ⁻¹)	ΔE_{prot} (kcal/mol)
SB1(imine)	-9.00	-5.81	3.19	3.24	7.41	1.60	0.63	-249.86
SB1(tertiary amine)	-8.46	-4.93	3.53	16.52	6.69	1.77	0.57	-208.89
SB2 (imine)	-8.95	-5.75	3.20	4.02	7.35	1.60	0.63	-242.78
SB2 (tertiary amine)	-8.28	-4.91	3.37	17.70	6.60	1.69	0.59	-209.10
SB3 (imine)	-8.83	-5.71	3.12	6.22	7.27	1.56	0.64	-256.19
SB3 (tertiary amine)	-8.20	-4.84	3.36	13.87	6.52	1.68	0.59	-214.38

**Figure 15.** (a) Vertical and (b) horizontal view of the optimized Structures of the SB2 molecule protonated on different heteroatoms. Colors of atoms are: gray (carbon), blue (nitrogen) and white (hydrogen).

there were structural changes, especially in the protonation of the tertiary amines (Figure 15). The nitrogen of the imine group showed the highest protonation energy (Table 10) from all inhibitors, forming a more stable conjugated acid.

Table 10 shows the quantum parameters for the protonated inhibitors. The increase in E_{HOMO} was observed for all protonated inhibitors, demonstrating that the adsorption of the inhibitors to the metallic surface will be favored in an acidic medium. In addition, the E_{LUMO} energy also increased for all inhibitors, indicating that the compounds act as more effective electron receptors in acidic medium. The dipole moment (μ) after protonation of the imine group indicates that molecular polarity can be classified as $\text{SB3} > \text{SB2} > \text{SB1}$. Values for bandgap, hardness, and softness were similar for all inhibitors in acid phase.

Therefore, in acid medium the anticorrosion potential of SB1, SB2, and SB3 improved considerably. This suggests that

in both neutral and acidic mediums, the functioning of the corrosion inhibitors is linked to their structures. Moreover, the compounds become more planar after protonation of the imine nitrogen, but the ethyl group still limits the adsorption of SB3 on the metallic surface. Finally, according to the theoretical results, inhibitors SB1 and SB2 present greater potential as corrosion inhibitors for steel, especially in acidic media.

4. Conclusions

The performance of three novel Schiff bases (SB) to inhibit corrosion on API P110 carbon steel was investigated. The spectroscopic analysis (FTIR and ¹H-NMR) confirmed that an efficient synthetical method was applied. Gravimetric tests performed in 1 M HCl over a 303K-333K temperature range confirmed the inhibition of steel corrosion. The SBs chemical structures are similar, differing by the type of substituent in the aromatic ring. For SB1, no substituent; SB2, ortho-methyl substituted; and SB3, para-ethyl substituted. SB1 performed better in gravimetric tests, and also showed the effect of temperature-concentration dependence. Raising concentration from 100 ppm to 600 ppm increased efficiency from 78.6% to 92.3% at 318 K. Combining these compounds with an ethoxylated lauryl alcohol, a surfactant, reached a maximum efficiency of 93%. The surface analysis revealed the reduced roughness and pit depths of carbon steel in inhibited samples by optical and scanning electron microscopies. Theoretical study through Density-functional theory (DFT) indicated the geometrical and the energetical similarities for the studied SBs in their neutral forms, but for the protonated species the conjugated acid is more stable and the frontier orbitals (especially HOMO) showed that adsorption would be favored compared to the neutral forms. The theoretical and experimental study highlighted that the presence of ethyl substituent can decrease adsorption and consequently the inhibitory performance as observed for SB3.

5. Acknowledgement

The authors would like to thank the Laboratory of Instruments and Research of the Department of Inorganic Chemistry of the Institute of Chemistry at the Federal University of Rio de Janeiro (UFRJ) for the FTIR analyses and E. Miguez for the ¹H-NMR analysis.

6. References

- Benarioua M, Mihi A, Bouzeghaia N, Naoun M. Mild steel corrosion inhibition by Parsley (*Petroselinum Sativum*) extract in acidic media. *Egypt J Pet.* 2019;28(2):155-9.

2. Ramezanzadeh M, Bahlakeh G, Ramezanzadeh B, Sanaei Z. Adsorption mechanism and synergistic corrosion-inhibiting effect between the green Nettle leaves extract and Zn^{2+} cations on carbon steel. *J Ind Eng Chem.* 2019;77:323-43.
3. Odewunmi NA, Umoren SA, Gasem ZM. Utilization of watermelon rind extract as a green corrosion inhibitor for mild steel in acidic media. *J Ind Eng Chem.* 2015;21:239-47.
4. Ouici H, Tourabi M, Benali O, Selles C, Jama C, Zarrouk A, et al. Adsorption and corrosion inhibition properties of 5-amino 1,3,4-thiadiazole-2-thiol on the mild steel in hydrochloric acid medium: Thermodynamic, surface and electrochemical studies. *J Electroanal Chem.* 2017;803:125-34.
5. Keramatinia M, Ramezanzadeh B, Mahdavian M. Green production of bioactive components from herbal origins through one-pot oxidation/polymerization reactions and application as a corrosion inhibitor for mild steel in HCl solution. *J Taiwan Inst Chem Eng.* 2019;105:134-49.
6. Bahlakeh G, Ramezanzadeh B, Dehghani A, Ramezanzadeh M. Novel cost-effective and high-performance green inhibitor based on aqueous Peganum harmala seed extract for mild steel corrosion in HCl solution: detailed experimental and electronic/atomic level computational explorations. *J Mol Liq.* 2019;283:174-95.
7. Umoren SA, Solomon MM, Obot IB, Suleiman RK. A critical review on the recent studies on plant biomaterials as corrosion inhibitors for industrial metals. *J Ind Eng Chem.* 2019;76:91-115.
8. Farahati R, Ghaffarinejad A, Mousavi-Khoshdel SM, Rezanian J, Behzadi H, Shokravi A. Synthesis and potential applications of some thiazoles as corrosion inhibitor of copper in 1 M HCl: experimental and theoretical studies. *Prog Org Coat.* 2019;132:417-28.
9. Solomon MM, Umoren SA, Quraishi MA, Salman M. Myristic acid based imidazoline derivative as effective corrosion inhibitor for steel in 15% HCl medium. *J Colloid Interface Sci.* 2019;551:47-60.
10. Liang C, Liu Z, Liang Q, Han GC, Han J, Zhang S, et al. Synthesis of 2-aminofluorene bis-Schiff base and corrosion inhibition performance for carbon steel in HCl. *J Mol Liq.* 2019;277:330-40.
11. Elemike EE, Nwankwo HU, Onwudiwe DC, Hosten EC. Synthesis, crystal structures, quantum chemical studies and corrosion inhibition potentials of 4-((4-ethylphenyl)imino methyl)phenol and (E)-4-((naphthalen-2-ylimino) methyl) phenol Schiff bases. *J Mol Struct.* 2017;1147:252-65.
12. Satpati S, Suhasaria A, Ghosal S, Saha A, Dey S, Sukul D. Amino acid and cinnamaldehyde conjugated Schiff bases as proficient corrosion inhibitors for mild steel in 1 M HCl at higher temperature and prolonged exposure: detailed electrochemical, adsorption and theoretical study. *J Mol Liq.* 2021;324:115077.
13. Okey NC, Obasi NL, Ejikeme PM, Ndinteh DT, Ramasami P, Sherif ESM, et al. Evaluation of some amino benzoic acid and 4-aminoantipyrine derived Schiff bases as corrosion inhibitors for mild steel in acidic medium: Synthesis, experimental and computational studies. *J Mol Liq.* 2020;315:113773.
14. Aatioui AE, Koudad M, Chelfi T, Erkan S, Azzouzi M, Aouniti A, et al. Experimental and theoretical study of new Schiff bases based on imidazo(1,2-a)pyridine as corrosion inhibitor of mild steel in 1M HCl. *J Mol Struct.* 2021;1226:129372.
15. Elemike EE, Nwankwo HU, Onwudiwe DC, Hosten EC. Synthesis, structures, spectral properties and DFT quantum chemical calculations of (E)-4-((4-propylphenyl)imino)methyl phenol and (E)-4-((2-tolylimino)methyl)phenol; their corrosion inhibition studies of mild steel in aqueous HCl. *J Mol Struct.* 2017;1141:12-22.
16. ASTM: American Society for Testing and Materials. ASTM G31-72. Guide for Laboratory Immersion Corrosion Testing of Metals [Internet]. West Conshohocken: ASTM International; 2004 [cited 2022 Apr 6]. Available from: <http://www.astm.org/cgi-bin/resolver.cgi?G31-72R04>
17. Bentrach H, Rahali Y, Chala A. Gum Arabic as an eco-friendly inhibitor for API 5L X42 pipeline steel in HCl medium. *Corros Sci.* 2014;82:426-31.
18. da Rocha JC, da Cunha Ponciano Gomes JA, D'Elia E. Corrosion inhibition of carbon steel in hydrochloric acid solution by fruit peel aqueous extracts. *Corros Sci.* 2010;52(7):2341-8.
19. Lee C, Yang W, Parr RG. Development of the Colle-Salvetti correlation-energy formula into a functional of the electron density. *Phys Rev B.* 1988;37(2):785-9.
20. Frisch MJ, Trucks G, Schlegel H, Scuseria G, Robb M, Cheeseman J, et al. Gaussian 16. Wallingford CT: Gaussian, Inc; 2016.
21. Pavia DL, Lampman GM, Kriz GS, Vyvyan JR. Introduction to spectroscopy. 5th ed. Stamford, CT: Cengage Learning; 2015. 690 p.
22. Elemike EE, Nwankwo HU, Onwudiwe DC. Experimental and theoretical studies of (Z)-N-(2-chlorobenzylidene) naphthalen-1-amine and (Z)-N-(3-nitrobenzylidene)naphthalen-1-amine, and their corrosion inhibition properties. *J Mol Struct.* 2018;1155:123-32.
23. Coates J. Interpretation of infrared spectra, a practical approach. In: Meyers RA, editor. Encyclopedia of analytical chemistry [Internet]. Chichester, UK: John Wiley & Sons, Ltd; 2006 [cited 2022 Apr 6]. p. a5606. Available from: <https://onlinelibrary.wiley.com/doi/10.1002/9780470027318.a5606>
24. Furtado LB, Nascimento RC, Seidl PR, Guimarães MJOC, Costa LM, Rocha JC, et al. Eco-friendly corrosion inhibitors based on Cashew nut shell liquid (CNSL) for acidizing fluids. *J Mol Liq.* 2019;284:393-404.
25. Kooliyat R, Kakkassery JT, Raphael VP, Cheruvathur SV, Paulson BM. Synthesis, cyclic voltammetric, electrochemical, and gravimetric corrosion inhibition investigations of schiff base derived from 5,5-Dimethyl-1,3-cyclohexanedione and 2-aminophenol on mild steel in 1 M HCl and 0.5 M H_2SO_4 . *Int J Electrochem.* 2019;2019:1-13.
26. Abd El-Lateef HM, Soliman KA, Tantawy AH. Novel synthesized Schiff Base-based cationic gemini surfactants: electrochemical investigation, theoretical modeling and applicability as biodegradable inhibitors for mild steel against acidic corrosion. *J Mol Liq.* 2017;232:478-98.
27. Elemike EE, Nwankwo HU, Onwudiwe DC. Synthesis and comparative study on the anti-corrosion potentials of some Schiff base compounds bearing similar backbone. *J Mol Liq.* 2019;276:233-42.
28. Li XL, Xie B, Feng JS, Lai C, Bai XX, Li T, et al. 2-Pyridinecarboxaldehyde-based Schiff base as an effective corrosion inhibitor for mild steel in HCl medium: experimental and computational studies. *J Mol Liq.* 2022;345:117032.
29. Guo W, Talha M, Lin Y, Kong X. Schiff's base with center of symmetry as an effective corrosion inhibitor for mild steel in acid medium: electrochemical & simulation studies. *Colloids Surf A Physicochem Eng Asp.* 2021;615:126234.
30. Chauhan DS, Mazumder MAJ, Quraishi MA, Ansari KR, Suleiman RK. Microwave-assisted synthesis of a new Piperonal-Chitosan Schiff base as a bio-inspired corrosion inhibitor for oil-well acidizing. *Int J Biol Macromol.* 2020;158:231-43.
31. Khadam AA. Effect of temperature on corrosion inhibition of copper - nickel alloy by tetraethylenepentamine under flow conditions. *J Chil Chem Soc.* 2014;59(3):2545-9.
32. Obot IB, Umoren SA, Obi-Egbedi NOJ. Corrosion inhibition and adsorption behaviour for aluminium by extract of *Anigeria robusta* in HCl solution: synergistic effect of iodide ion. *J Mater Environ Sci.* 2011;2(1):49-60.
33. Gowraraju ND, Jagadeesan S, Ayyasamy K, Olasunkanmi LO, Ebenso EE, Subramanian C. Adsorption characteristics of Iota-carrageenan and Inulin biopolymers as potential corrosion

- inhibitors at mild steel/sulphuric acid interface. *J Mol Liq.* 2017;232:9-19.
34. Karthikaiselvi R, Subhashini S. The water soluble composite poly(vinylpyrrolidone–methylaniline): A new class of corrosion inhibitors of mild steel in hydrochloric acid media. *Arab J Chem.* 2017;10:S627-35.
 35. Shahabi S, Hamidi S, Ghasemi JB, Norouzi P, Shakeri A. Synthesis, experimental, quantum chemical and molecular dynamics study of carbon steel corrosion inhibition effect of two Schiff bases in HCl solution. *J Mol Liq.* 2019;285:626-39.
 36. Tharial Xavier G, Thirumalairaj B, Jaganathan M. Effect of Piperidin-4-ones on the corrosion inhibition of mild steel in 1 N H₂SO₄. *Int J Corros.* 2015;2015:1-15.
 37. Goyal M, Kumar S, Bahadur I, Verma C, Ebenso EE. Organic corrosion inhibitors for industrial cleaning of ferrous and non-ferrous metals in acidic solutions: a review. *J Mol Liq.* 2018;256:565-73.
 38. Trabaneli G. Inhibitors for chemical cleaning treatments in corrosion inhibitors. London: The Institute of Materials; 1994.
 39. Wang C, Chen J, Han J, Wang C, Hu B. Enhanced corrosion inhibition performance of novel modified polyaspartic acid on carbon steel in HCl solution. *J Alloys Compd.* 2019;771:736-46.
 40. Badr EA, Bedair MA, Shaban SM. Adsorption and performance assessment of some imine derivatives as mild steel corrosion inhibitors in 1.0 M HCl solution by chemical, electrochemical and computational methods. *Mater Chem Phys.* 2018;219:444-60.
 41. Fernandes CM, Alvarez LX, dos Santos NE, Maldonado Barrios AC, Ponzio EA. Green synthesis of 1-benzyl-4-phenyl-1H-1,2,3-triazole, its application as corrosion inhibitor for mild steel in acidic medium and new approach of classical electrochemical analyses. *Corros Sci.* 2019;149:185-94.
 42. Bedair MA, Soliman SA, Bakr MF, Gad ES, Lgaz H, Chung IM, et al. Benzidine-based Schiff base compounds for employing as corrosion inhibitors for carbon steel in 1.0 M HCl aqueous media by chemical, electrochemical and computational methods. *J Mol Liq.* 2020;317:114015.
 43. Finšgar M, Jackson J. Application of corrosion inhibitors for steels in acidic media for the oil and gas industry: a review. *Corros Sci.* 2014;86:17-41.
 44. Zehra S, Mobin M, Aslam J, Parveen M. Assessment of glycine derivative N-benzylidene-2((2-oxo-2-(10H-phenothiazine-10yl) ethyl)amino) acetohydrazide as inhibitor for mild steel corrosion in 1 M HCl solution: electrochemical and theoretical approach. *J Adhes Sci Technol.* 2018;32(3):317-42.
 45. Rodríguez-Torres A, Valladares-Cisneros MG, Saldaña Heredia A, González-Rodríguez JG. KI effects on corrosion inhibition for 1018 steel in acid media using *Medicago sativa*. *Front Chem.* 2022;10:1-12.
 46. Obot IB, Umoren SA, Obi-Egbedi NO. Corrosion inhibition and adsorption behaviour for aluminium by extract of *Aningeria robusta* in HCl solution: synergistic effect of iodide ions. *J Mater Environ Sci.* 2011;2:60-71.
 47. Oguzie EE. Evaluation of the inhibitive effect of some plant extracts on the acid corrosion of mild steel. *Corros Sci.* 2008;50(11):2993-8.
 48. Behpour M, Ghoreishi SM, Gandomi-Niasar A, Soltani N, Salavati-Niasari M. The inhibition of mild steel corrosion in hydrochloric acid media by two Schiff base compounds. *J Mater Sci.* 2009;44(10):2444-53.
 49. Jamal ANA, Anwar SM. Comparative study of N-[4-methoxyphenyl] (morpholin-4-yl)methyl]acetamide (MMPA) and N-[morpholin-4-yl(phenyl)methyl]acetamide (MPA) as corrosion inhibitors for mild steel in sulfuric acid solution. *Arab J Chem.* 2017;10:S261-73.
 50. Ben Aoun S. On the corrosion inhibition of carbon steel in 1 M HCl with a pyridinium-ionic liquid: chemical, thermodynamic, kinetic and electrochemical studies. *RSC Advances.* 2017;7(58):36688-96.
 51. Benabdellah M, Tounsi A, Khaled KF, Hammouti B. Thermodynamic, chemical and electrochemical investigations of 2-mercapto benzimidazole as corrosion inhibitor for mild steel in hydrochloric acid solutions. *Arab J Chem.* 2011;4(1):17-24.
 52. Singh AK. Inhibition of mild steel corrosion in hydrochloric acid Solution by 3-(4-((Z) -Indolin-3-ylideneamino)phenylimino) indolin-2-one. *Ind Eng Chem Res.* 2012;51(8):3215-23.
 53. Hameed RSA. Ranitidine drugs as non-toxic corrosion inhibitors for mild steel in hydrochloric acid medium. *Port Electrochem Acta.* 2011;29(4):273-85.
 54. Murmu M, Saha SKr, Murmu NC, Banerjee P. Effect of stereochemical conformation into the corrosion inhibitive behaviour of double azomethine based Schiff bases on mild steel surface in 1 mol L⁻¹ HCl medium: an experimental, density functional theory and molecular dynamics simulation study. *Corros Sci.* 2019;146:134-51.
 55. dos Santos ÉC, Cordeiro R, Santos M, Rodrigues PRP, Singh A, D'Elia E. Barley Agro-industrial residues as corrosion inhibitor for mild steel in 1mol L⁻¹HCl solution. *Mater Res.* 2019;22(2):e20180511.
 56. Ahamed KR, Farzana BA, Diraviam SJ, Dorothy R, Rajendran S, Al-Hashem A. Electrochemical characterization of catechol-dimethylamine adduct at different pH values. *Port Electrochem Acta.* 2019;37(1):51-70.
 57. Saha SKr, Banerjee P. Introduction of newly synthesized Schiff base molecules as efficient corrosion inhibitors for mild steel in 1 M HCl medium: an experimental, density functional theory and molecular dynamics simulation study. *Mater Chem Front.* 2018;2(9):1674-91.
 58. Khadom AA, Abd AN, Ahmed NA. Xanthium strumarium leaves extracts as a friendly corrosion inhibitor of low carbon steel in hydrochloric acid: kinetics and mathematical studies. *S Afr J Chem Eng.* 2018;25:13-21.
 59. Jüttner K. Electrochemical impedance spectroscopy (EIS) of corrosion processes on inhomogeneous surfaces. *Electrochim Acta.* 1990;35(10):1501-8.
 60. Kumar R, Yadav OS, Singh G. Electrochemical and surface characterization of a new eco-friendly corrosion inhibitor for mild steel in acidic media: a cumulative study. *J Mol Liq.* 2017;237:413-27.
 61. Gerengi H, Sen N, Uygur I, Solomon MM. Corrosion response of ultra-high strength steels used for automotive applications. *Mater Res Express.* 2019;6:0865a6.
 62. Badea GE, Caraban A, Sebesan M, Zitac S, Cret P, Setel A. Polarisation measurements used for corrosion rates determination. *J Sustain Energy.* 2010;1(1):1-4.
 63. Furtado LB, Nascimento RC, Guimarães MJOC, Henrique FJFS, Rocha JC, Seidl PR, et al. Cleaner corrosion inhibitors using Peumus boldus Molina formulations in oil well acidizing fluids: gravimetric, electrochemical and DFT studies. *Sustain Chem Pharm.* 2021;19:100353.
 64. Dehghani A, Bahlakeh G, Ramezanzadeh B. A detailed electrochemical/theoretical exploration of the aqueous Chinese gooseberry fruit shell extract as a green and cheap corrosion inhibitor for mild steel in acidic solution. *J Mol Liq.* 2019;282:366-84.
 65. Sedik A, Lerari D, Salci A, Athmani S, Bachari K, Gecibesler İH, et al. Dardagan Fruit extract as eco-friendly corrosion inhibitor for mild steel in 1 M HCl: electrochemical and surface morphological studies. *J Taiwan Inst Chem Eng.* 2020;107:189-200.
 66. Chen S, Chen S, Zhu B, Huang C, Li W. Magnolia grandiflora leaves extract as a novel environmentally friendly inhibitor for Q235 steel corrosion in 1 M HCl: combining experimental and theoretical researches. *J Mol Liq.* 2020;311:113312.

67. Njoku DI, Njoku CN, Lgaz H, Okafor PC, Oguzie EE, Li Y. Corrosion protection of Q235 steel in acidic-chloride media using seed extracts of Piper guineense. *J Mol Liq.* 2021;330:115619.
68. Shaban SM, Aiad I, El-Sukkary MM, Soliman EA, El-Awady MY. Evaluation of some cationic surfactants based on dimethylaminopropylamine as corrosion inhibitors. *J Ind Eng Chem.* 2015;21:1029-38.
69. Murulana LC, Kabanda MM, Ebenso EE. Investigation of the adsorption characteristics of some selected sulphonamide derivatives as corrosion inhibitors at mild steel/hydrochloric acid interface: Experimental, quantum chemical and QSAR studies. *J Mol Liq.* 2016;215:763-79.
70. ASTM: American Society for Testing and Materials. ASTM G46-94. Guide for Examination and Evaluation of Pitting Corrosion [Internet]. West Conshohocken: ASTM International; 2005 [cited 2022 Apr 7]. Report No.: G46-94. Available from: <http://www.astm.org/cgi-bin/resolver.cgi?G46-94R05>
71. Furtado LB, Nascimento RC, Henrique FJFS, Guimarães MJOC, Rocha JC, Ponciano JAC, et al. Effects of temperature, concentration and synergism on green Schiff bases synthesized from vanillin in applications as corrosion inhibitors for carbon steel in well stimulation. *J Petrol Sci Eng.* 2022;213:110401.